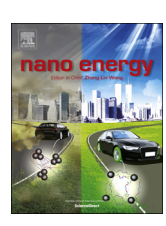
FISEVIER

#### Contents lists available at ScienceDirect

## Nano Energy

journal homepage: www.elsevier.com/locate/nanoen



## Full paper

# *In situ* Raman study of nickel bicarbonate for high-performance energy storage device



Shuge Dai<sup>a,b,\*</sup>, Zhuangfei Zhang<sup>a</sup>, Junmin Xu<sup>a</sup>, Weixia Shen<sup>a</sup>, Qiaobao Zhang<sup>d</sup>, Xigui Yang<sup>a</sup>, Tingting Xu<sup>a</sup>, Dai Dang<sup>b</sup>, Hao Hu<sup>b</sup>, Bote Zhao<sup>b</sup>, Ye Wang<sup>a</sup>, Chong Qu<sup>b</sup>, Jianwei Fu<sup>b</sup>, Xinjian Li<sup>a</sup>, Chenguo Hu<sup>c,\*\*</sup>, Meilin Liu<sup>b,\*\*\*</sup>

- a Key Laboratory of Material Physics of Ministry of Education, School of Physics and Engineering, Zhengzhou University, Zhengzhou, 450052, PR China
- <sup>b</sup> School of Materials Science and Engineering, Georgia Institute of Technology, Atlanta, GA, 30332-0245, USA
- <sup>c</sup> Department of Applied Physics, Chongqing University, Chongqing, 400044, PR China

#### ARTICLE INFO

#### Keywords: Nickel bicarbonate Charge storage mechanism In situ Raman spectroscopy Hybrid supercapacitor

#### ABSTRACT

In situ Raman spectroscopy is a powerful technique for probing the structure and phase composition of the electrode materials that are undergoing charge-discharge process. Herein, the charge storage mechanism of asprepared Ni(HCO<sub>3</sub>)<sub>2</sub> nanomaterial is successfully studied by using the *in situ* Raman spectroscopy. The charge storage can be attributed to the deep oxidation of Ni<sup>2+</sup> into Ni<sup>3+</sup>, and the irreversible phase transformation of  $\gamma$ -NiOOH into disordered  $\beta$ -Ni(OH)<sub>2</sub> damages the crystal structure of Ni(HCO<sub>3</sub>)<sub>2</sub>, arousing the capacity loss of the electrode during the long-term cycling process. Under the guidance of the experimental investigations, a porous Ni(HCO<sub>3</sub>)<sub>2</sub>/reduced graphene oxide (rGO) nanocomposite is designed and synthesized, exhibiting ultrahigh specific capacity (846 C g<sup>-1</sup>) and excellent rate capability (618 C g<sup>-1</sup> at 20 A g<sup>-1</sup>). When coupled with an negative electrode based on rGO, the resulting hybrid supercapacitor shows an ultrahigh energy density of 66 Wh kg<sup>-1</sup> at power density of 1.9 kW kg<sup>-1</sup> and good cycling stability. These findings provide important insight into the mechanism of charge storage, and scientific basis for design of high-performance energy storage materials.

## 1. Introduction

Understanding the fundamental energy storage and conversion mechanism is vital to optimizing the performance of energy storage devices, and to rationally designing novel electrode materials with desired properties [1–4]. Recently, transition-metal carbonates (MCO $_3$ ; M = Ni, Co, Fe, and Mn) have been widely recognized as attractive electrode materials for energy storage owing to their high theoretical capacities, superior stability and lower cost [5–8]. Among these electrode materials, nickel bicarbonate (Ni(HCO $_3$ ) $_2$ ) have attracted intense interest owing to its high theoretical capacity (1780 mAh g $^{-1}$ ), natural abundance, and environmental friendliness [7–9]. However, most of the reported materials display unsatisfactory rate capability and poor cycling stability due to the phase changes associated with Faradic reactions during the charge-discharge process. To solve these problems, a profound understanding of the charge storage mechanism is very

important, which is the scientific basis for rational construction of new materials or composite structures with outstanding performance.

Recently, the use of *in situ* techniques, such as *in situ* X-ray diffraction (XRD), *in situ* X-ray absorption spectroscopy (XAS), *in situ* transmission electron microscopy (TEM) and *in situ* Raman spectroscopy, make it possible to directly probe structural changes of electrode materials at different stages during the electrochemical reaction process under a wide range of testing conditions [3,10–12]. Among these test techniques, Raman spectroscopy is a powerful tool for revealing the vital structural and chemical properties of electrode materials, especially when properly combined with theoretical vibrational analyse [13–15]. *In situ* Raman spectroscopy have been successfully applied to probing subtle structural evolution of electrode materials during the electrochemical cycling process, which offers critical insights into the mechanism of charge storage and conversion in the electrode materials because the evolution of a Raman peak can be directly linked to a

E-mail addresses: shugedai@zzu.edu.cn (S. Dai), hucg@cqu.edu.cn (C. Hu), meilin.liu@mse.gatech.edu (M. Liu).

d Department of Materials Science and Engineering, College of Materials, Xiamen University, Xiamen, Fujian, 361005, PR China

<sup>\*</sup>Corresponding author. Key Laboratory of Material Physics of Ministry of Education, and School of Physics and Engineering, Zhengzhou University, Zhengzhou, 450052, PR China.

<sup>\*\*</sup> Corresponding author.

<sup>\*\*\*</sup> Corresponding author.

specific structural change [3,16].

To profound understanding of the energy storage mechanism of Ni (HCO<sub>3</sub>)<sub>2</sub>, we used in situ Raman spectroscopy to study the local structure of Ni(HCO<sub>3</sub>)<sub>2</sub>, including the charge and orbital ordering, the effects of phase transitions and oxygen disorder effects. The Raman spectra revealed a reversible redox reaction between Ni(HCO<sub>3</sub>)<sub>2</sub> and γ-NiOOH, and the high specific capacity of Ni(HCO<sub>3</sub>)<sub>2</sub> could be attributed to the deep oxidation of Ni<sup>2+</sup> into Ni<sup>3+</sup> and the reversible reaction. However, it also demonstrated that there was an electrochemically induced phase transformation of Ni(HCO<sub>3</sub>)<sub>2</sub> during the long redox reaction process. The phase transition of γ-NiOOH into disordered β-Ni(OH)<sub>2</sub> directly destroyed the structure of the Ni(HCO<sub>3</sub>)<sub>2</sub> electrode, thus arousing the poor cycling stability. To overcome these defects, we have designed a composite with graphene incorporating into the Ni(HCO<sub>3</sub>)<sub>2</sub> material. The optimized Ni(HCO<sub>3</sub>)<sub>2</sub>/reduced graphene oxide (Ni(HCO<sub>3</sub>)<sub>2</sub>/rGO) nanocomposite electrode exhibited excellent rate capability (~73% capacity retention as the current was increase from 1 to 20 A g<sup>-1</sup>) and good cycling stability. Moreover, we have also fabricated a high performance hybrid supercapacitor device based on the Ni(HCO3)2/rGO nanocomposite, which demonstrated a high energy density and power density, revealing its potential applications.

#### 2. Experimental section

#### 2.1. Synthesis of Ni(HCO<sub>3</sub>)<sub>2</sub> nanospheres

First, 1 mmol of NiCl $_2$ -6H $_2$ O and 5 mmol of ureal (CH $_4$ N $_2$ O) were dissolved in deionized water (10 mL) and ethanol solution (5 mL). Then the mixed solution was retained at 150 °C for 12 h. After cooled down to room temperature, the product was rinsed with ultrapure water, and dried under vacuum at 60 °C overnight.

### 2.2. Synthesis of Ni(HCO<sub>3</sub>)<sub>2</sub>/rGO composite

Graphene oxide (GO) was synthesized by using an improved Hummers' method [17]. The Ni(HCO $_3$ ) $_2$ /rGO nanocomposite was achieved via a hydrothermal process. Briefly, 1 mmol of NiCl $_2$ 6H $_2$ O and 5 mmol of ureal were dissolved in 5 mL of ethanol and 10 mL of GO solution (2 mg mL $^{-1}$ ) under stirring for 1 h. Then the mixed solution was retained at 150 °C for 12 h. After cooled down to room temperature, the product was rinsed with ultrapure water, and dried under vacuum at 60 °C overnight.

#### 2.3. Characterization

The morphology of prepared samples were characterized by using a scanning electron microscopy (JEOL JSM-6700F), transmission electron microscopy (FEI Talso 200s). The composition of prepared samples were measured by using X-ray diffraction (XRD) with Cu Ka radiation ( $\lambda=1.5418\,\text{Å}$ ). The specific surface area of prepared samples were measured via the Brunauer-Emmett-Teller method  $N_2$  adsorption/desorption experiments at 77 K after preheating at 100 °C for 24 h. In situ Raman spectra were obtained using a LabRAM HR evolution system and

the 532 nm line of a diode-pumped solid state laser while a cyclic voltammetry (CV) test in a three-electrode cell was run at a scan rate of 2 mV s  $^{-1}$  (IviumStat.h). The beam was focused to a spot size of about 2.6 µm, and the output power of the laser was set to 10 mW. *In situ* electrochemical impedance spectra (EIS) were obtained using a VMP3 electrochemical workstation (Bio-Logic, Claix, France) while the galvanostatic charge/discharge (GCD) test in a three-electrode cell was run at a current density of  $4\,\mathrm{A\,g}^{-1}$ .

## 2.4. Electrochemical performance evaluation

Cyclic voltammetry, galvanostatic charge/discharge and electrochemical impedance spectroscopy tests were measured on cells at room temperature. The working electrode was made from the mixture of Ni (HCO<sub>3</sub>)<sub>2</sub>/rGO nanocomposite, Super P Li powders, and polytetra-fluoroethylene (PTFE) binder at a weight ratio of 8:1:1 with assistance of ethanol. The PTFE was dissolved in deionized water before using. The working electrode was achieved by pressing the films between two nickel foams. The effective mass loading of active material is about 3.5–4 mg cm<sup>-2</sup>. The specific galvanostatic capacity (*C*) of the electrodes should be achieved by the following equation [18]:

$$C = It/m \tag{1}$$

where t (s) is the discharge time, m (mg) is the effective mass of active electrode material and I (mA) is the discharge current.

A hybrid supercapacitor was constructed from the Ni(HCO<sub>3</sub>)<sub>2</sub>/rGO and rGO films. The specific capacitance C (F g<sup>-1</sup>) of the HSCs was achieved by the following equation [19,20]:

$$C = \frac{2i_m \int V dt}{V^2} | \frac{V_f}{V_i}$$
 (2)

where  $i_m = I/m$  (A g<sup>-1</sup>) is the current density, I is the discharge current, m is the total mass of Ni(HCO<sub>3</sub>)<sub>2</sub>/rGO composite and rGO, V is the potential with an initial and final value of  $V_i$  and  $V_f$  respectively.

The energy and power densities of the HSCs were achieved by the following equations [21]:

$$E = \frac{I \int V dt}{m} \tag{3}$$

$$P = \frac{3600E}{t} \tag{4}$$

where t (s) is the discharge time, I is the discharge current, V is the cell voltage, dt is the time differential, and m is the total mass of Ni (HCO<sub>3</sub>)<sub>2</sub>/rGO composite and rGO.

## 3. Results and discussion

The synthesis procedure of Ni(HCO<sub>3</sub>)<sub>2</sub>/rGO composite electrode is illustrated in Fig. 1. Briefly, the Ni(HCO<sub>3</sub>)<sub>2</sub> nanoparticles were grown onto rGO sheets by adding the NiCl<sub>2</sub> and CH<sub>4</sub>N<sub>2</sub>O into the GO suspension via a low-temperature hydrothermal condition. The morphology and microstructure of the as-synthesized samples were first examined by field-emission scanning electron microscopy (SEM).

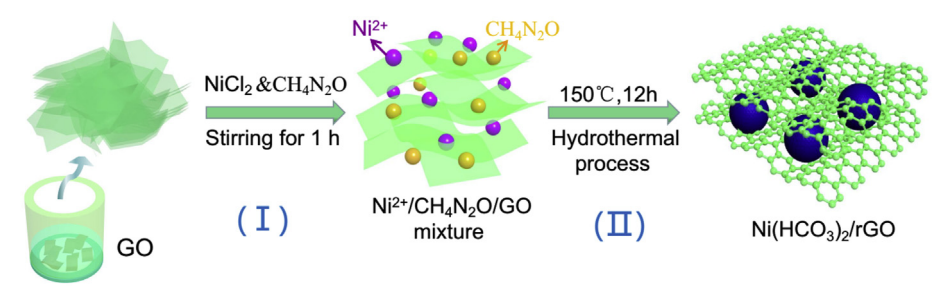


Fig. 1. Schematic illustration of synthesis processes of Ni(HCO<sub>3</sub>)<sub>2</sub>/rGO composite.

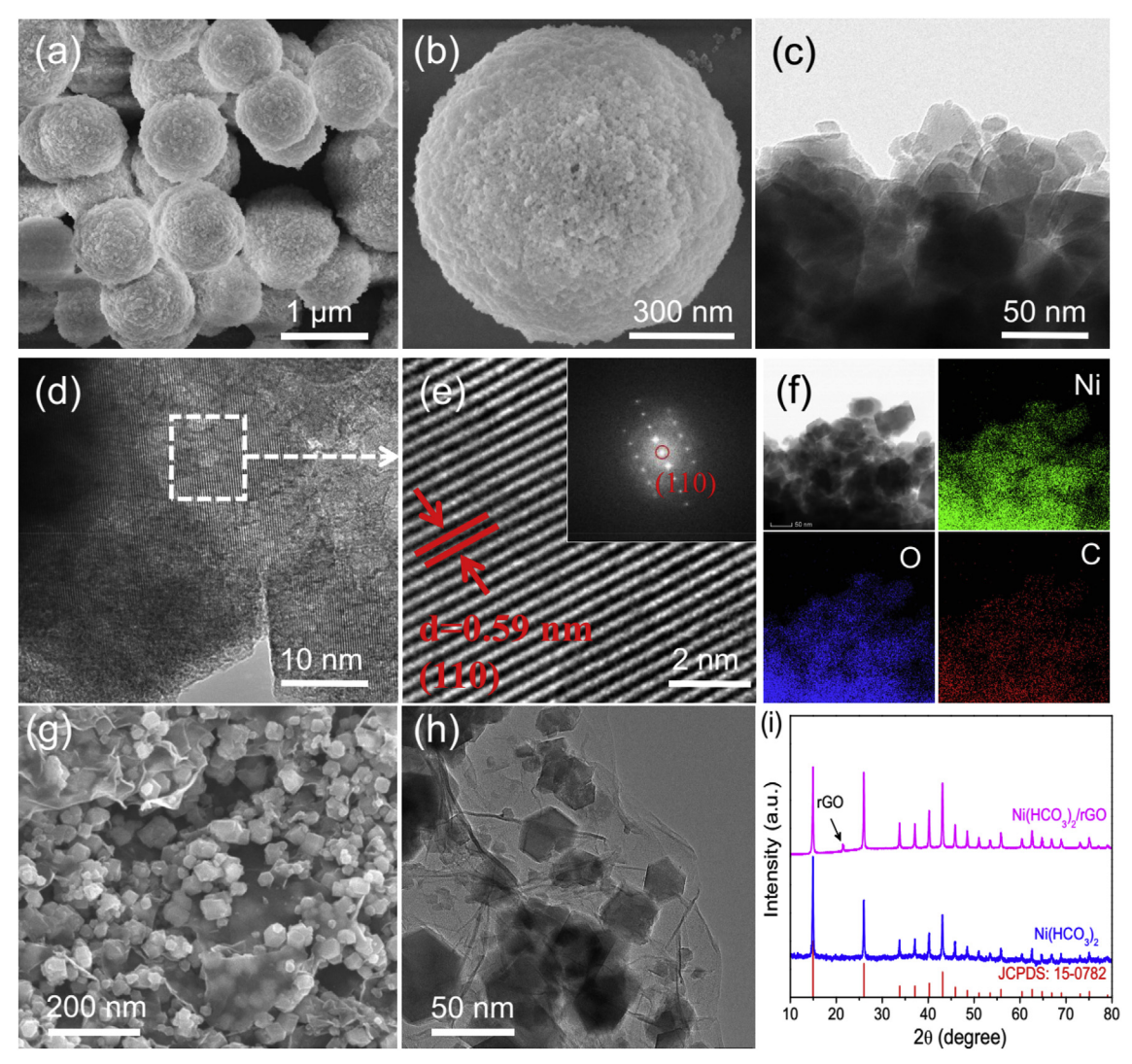


Fig. 2. (a,b) SEM images of synthesized Ni(HCO<sub>3</sub>)<sub>2</sub> microspheres. (c) TEM and HRTEM (d,e) images of synthesized Ni(HCO<sub>3</sub>)<sub>2</sub> microspheres. (f) TEM-EDX mapping images of synthesized Ni(HCO<sub>3</sub>)<sub>2</sub> microspheres. (g) SEM and (h) TEM images of Ni(HCO<sub>3</sub>)<sub>2</sub>/rGO composite. (i) XRD patterns of Ni(HCO<sub>3</sub>)<sub>2</sub> microspheres and Ni (HCO<sub>3</sub>)<sub>2</sub>/rGO composite.

Fig. 2a and b clearly show the morphology of nanoparticles assembled into solid spheres with an average diameter of 1  $\pm$  0.3  $\mu$ m, which is further proved by TEM analysis (Fig. 2c).

The high-resolution transmission electron microscopy (HRTEM) images (Fig. 2d and e) of Ni(HCO<sub>3</sub>)<sub>2</sub> prove that these nanoparticles are highly crystallized structures with a lattice fringe spacing of 0.59 nm, which corresponds to the (110) plane of Ni(HCO<sub>3</sub>)<sub>2</sub>. Moreover, the TEM elemental mapping(Fig. 2f) of as-prepared Ni(HCO<sub>3</sub>)<sub>2</sub> reveals a relatively uniform distribution of Ni, C and O elements in the whole nanoparticles. For Ni(HCO<sub>3</sub>)<sub>2</sub>/rGO composite, the SEM images (Fig. 2g and Fig. S1a) show that the shape of Ni(HCO<sub>3</sub>)<sub>2</sub> is changed from regular solid microsphere into irregular nanoparticle. These nanoparticles with an average diameter of 20-50 nm homogeneously distribute in transparent rGO nanosheets. The TEM image (Fig. 2h) further demonstrates the intimate connection microstructure of Ni(HCO<sub>3</sub>)<sub>2</sub> nanoparticles and rGO nanosheets, and these irregular nanoparticles are well encapsulated within the wrinkled rGO nanosheets. Moreover, the HRTEM images (Figs. S1b and c) further prove that the Ni(HCO<sub>3</sub>)<sub>2</sub> nanoparticles anchored on the rGO nanosheets are well crystallized. It shows clear lattice fringe of 0.59 nm that corresponding to the d-spacing of the (110) plane of Ni(HCO<sub>3</sub>)<sub>2</sub>, which is in good agreement with the pure Ni (HCO<sub>3</sub>)<sub>2</sub> sample. These results can also be further proved by XRD results. As shown in Fig. 2i, the XRD pattern of as-prepared Ni(HCO<sub>3</sub>)<sub>2</sub>

sample shows a pure crystallographic feature of cubic Ni(HCO<sub>3</sub>)<sub>2</sub> crystals (JCPDS No. 15–0782). For Ni(HCO<sub>3</sub>)<sub>2</sub>/rGO composite, a new diffraction peak can be observed at about 23°, which can be assigned to the (002) plane of rGO [22]. The intensity of the diffraction peak of rGO is very weak, indicating a lower amount of rGO in the composite. It is expected that the rGO nanosheets can provide more active sites and effective ion transport paths, meanwhile, it can enhance the charge transfer kinetics and maintain structural integrity of the whole electrodes during the long charge-discharge cycling process.

The surface area and pore size distribution of as-prepared Ni (HCO<sub>3</sub>)<sub>2</sub> microspheres (Fig. 3a) and Ni(HCO<sub>3</sub>)<sub>2</sub>/rGO composite (Fig. 3b) were evaluated by nitrogen adsorption-desorption measurements, respectively. As shown in the inset of Fig. 3a, the Ni(HCO<sub>3</sub>)<sub>2</sub> microspheres possess an average pore diameter of 3.8 nm and pore volume of  $0.134 \, \mathrm{cm}^3 \, \mathrm{g}^{-1}$ . Moreover, the BET specific surface area of Ni (HCO<sub>3</sub>)<sub>2</sub>/rGO nanocomposite is calculated to be  $54 \, \mathrm{m}^2 \, \mathrm{g}^{-1}$ , which is larger than the Ni(HCO<sub>3</sub>)<sub>2</sub> microspheres (30  $\mathrm{m}^2 \, \mathrm{g}^{-1}$ ), revealing that the increased surface area may be related to the morphology change of Ni (HCO<sub>3</sub>)<sub>2</sub> microspheres and the incorporation of GO nanosheets. The composition and surface electronic state of the Ni(HCO<sub>3</sub>)<sub>2</sub> microspheres and Ni(HCO<sub>3</sub>)<sub>2</sub>/rGO composite were further analyzed by X-ray photoelectron spectroscopy (XPS) and the corresponding results are presented in Fig. 3c,d and Figs. S2a and b. The XPS survey scan spectrum

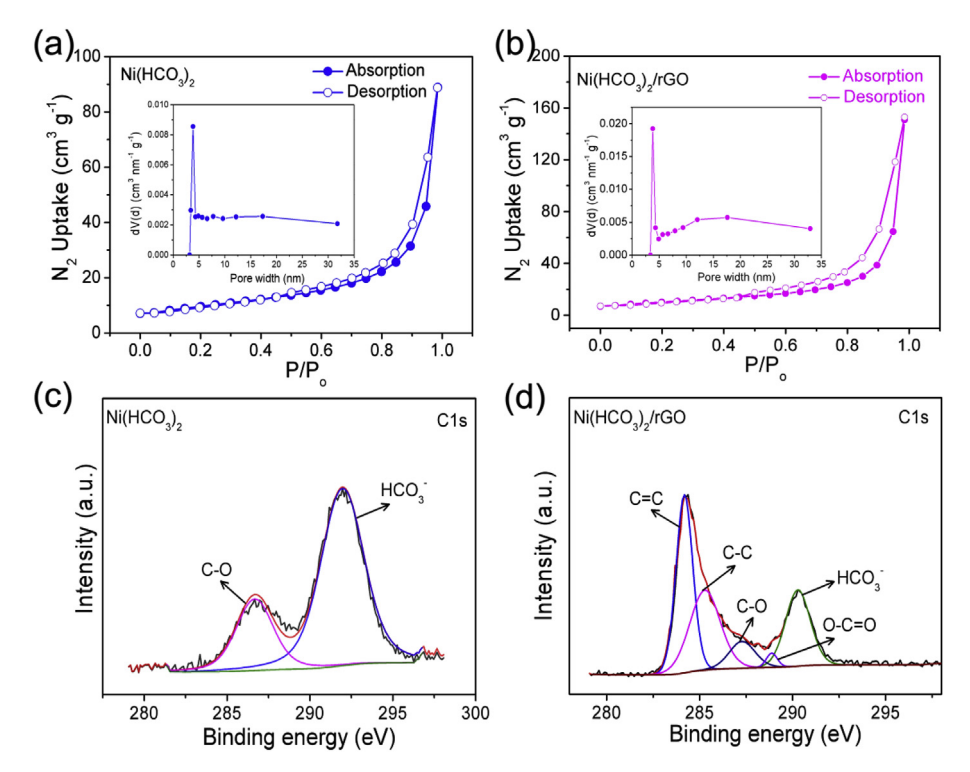


Fig. 3. The  $N_2$  absorption-desorption isotherms of the as-prepared (a) Ni(HCO<sub>3</sub>)<sub>2</sub>/rGO, and (b) Ni(HCO<sub>3</sub>)<sub>2</sub> powders, the inset is the corresponding pore distribution. XPS spectra of C1s in Ni(HCO<sub>3</sub>)<sub>2</sub> (c), and Ni(HCO<sub>3</sub>)<sub>2</sub>/rGO (d) samples.

shown in Fig. S2a indicates the presence of characteristic peaks of Ni, C and O elements. For the high-resolution spectrum of Ni 2p (Fig. S2b), two obvious shakeup satellites and the Ni  $2p_{3/2}$  and Ni  $2p_{1/2}$  peaks were observed at 858.2 and 876.5 eV, indicating the presence of Ni<sup>2+</sup> in the Ni(HCO<sub>3</sub>)<sub>2</sub> [23,24]. For Ni(HCO<sub>3</sub>)<sub>2</sub>/rGO composite, the high resolution spectrum of Ni 2p exhibits two peaks at 856.5 eV and 874.3 eV, as well as two satellite peaks, indicating the existence of Ni<sup>2+</sup> in the Ni (HCO<sub>3</sub>)<sub>2</sub>/rGO composite [7]. As shown in Fig. 3c, the C 1s region of Ni (HCO<sub>3</sub>)<sub>2</sub> shows two peaks at binding energies of 286.8 and 291.8 eV, which can be assigned to C–O and HCO<sub>3</sub><sup>-</sup> bindings, respectively [24]. However, the C 1s region of Ni(HCO<sub>3</sub>)<sub>2</sub>/rGO can be fitted to five peaks at binding energies of 284.2, 285.3, 287.3, 288.9 and 290.3 eV, which can be assigned to C=C, C-C, C-O, O-C=O and HCO<sub>3</sub><sup>-</sup> bindings, respectively [7,25–27]. These results further confirm the presence of Ni (HCO<sub>3</sub>)<sub>2</sub> in the nanocomposite.

The electrochemical behaviors of as-prepared Ni(HCO<sub>3</sub>)<sub>2</sub> and Ni (HCO<sub>3</sub>)<sub>2</sub>/rGO composite electrodes were first evaluated using a threeelectrode configuration. Presented in Fig. 4a are some typical CV curves of the Ni(HCO<sub>3</sub>)<sub>2</sub> microspheres and the Ni(HCO<sub>3</sub>)<sub>2</sub>/rGO nanocomposites at a scan rate of 10 mV s<sup>-1</sup>. The integral area of the Ni(HCO<sub>3</sub>)<sub>2</sub>/ rGO electrode is larger than that of Ni(HCO<sub>3</sub>)<sub>2</sub> microspheres, suggesting that the Ni(HCO<sub>3</sub>)<sub>2</sub>/rGO composite electrode has a higher specific capacity. Fig. 4b displays the CV curves of the Ni(HCO<sub>3</sub>)<sub>2</sub>/rGO composite electrode at various scan rates. The redox current increases and the shape of these curves is not obviously changed with the increasing of scan rate, suggesting that the unique architecture of Ni(HCO<sub>3</sub>)<sub>2</sub>/rGO is favorable for fast redox reaction. Fig. S3a and b demonstrate the dominance of diffusion-controlled electrode reaction, suggesting the energy storage in the hybrid electrode mainly depends on Faradic reaction. The corresponding CV curves of pure Ni(HCO<sub>3</sub>)<sub>2</sub> electrode is displayed in Fig. S4a. The GCD curves (Fig. 4c) are highly symmetric and show a discharge voltage plateau at about 0.2-0.3 V, revealing the nanocomposite has a good electrochemical characteristic and reversible redox reaction. The calculated specific capacity based on the discharge current density is shown in Fig. 4d. The corresponding GCD curves of the Ni(HCO<sub>3</sub>)<sub>2</sub> electrode are displayed in Fig. S4b. The Ni(HCO<sub>3</sub>)<sub>2</sub>/rGO

electrode delivered a high specific capacity of 846, 803, 763, 705, 685, 643 and 620 C g $^{-1}$  at 1–20 A g $^{-1}$ , which is larger than that of pure Ni (HCO $_3$ ) $_2$  electrode (738 C g $^{-1}$  at 1 A g $^{-1}$ ). Moreover,  $\sim$ 73%  $(620 \,\mathrm{G\,g^{-1}})$  of the specific capacity can be retained even at 20  $\mathrm{A\,g^{-1}}$ , revealing its excellent rate capability. To the best of our knowledge, the electrochemical performances of as-prepared Ni(HCO3)2/rGO nanocomposite is superior to those reported recently, such as Ni(HCO<sub>3</sub>)<sub>2</sub> nanocrystals  $(638 \,\mathrm{G\,g^{-1}})$  at  $2 \,\mathrm{A\,g^{-1}}$  [8], Ni(HCO<sub>3</sub>)<sub>2</sub>/GS  $(622 \,\mathrm{C\,g^{-1}})$  at  $2 \text{ A g}^{-1}$ ) [22], Ni(HCO<sub>3</sub>)<sub>2</sub>-PDA-rGO (788 C g<sup>-1</sup> at  $1 \text{ A g}^{-1}$ ) [23]. The good performance of the Ni(HCO<sub>3</sub>)<sub>2</sub>/rGO nanocomposite can be attributed to its unique nanocomposite structure. First, the Ni(HCO<sub>3</sub>)<sub>2</sub>/ rGO nanocomposite displays large specific surface area, which increases the electrode/electrolyte contact area and improves the availability of the electrode materials, greatly contributing to the enhancement of its specific capacity. Second, the rGO enhances the conductivity of Ni (HCO<sub>3</sub>)<sub>2</sub>/rGO nanocomposite. As shown in Fig. S5, the impedance loop for the Ni(HCO<sub>3</sub>)<sub>2</sub>/rGO composite electrode was smaller at high frequencies, suggesting faster charge transfer kinetics. Besides, the impedance tail for the Ni(HCO<sub>3</sub>)<sub>2</sub>/rGO composite electrode had larger slope than the pure Ni(HCO<sub>3</sub>)<sub>2</sub> electrode at low frequencies, which indicates faster ion diffusion near the interface of electrode/electrolyte, resulting in a significant increase in rate performance. Third, these Ni (HCO<sub>3</sub>)<sub>2</sub> nanoparticles were well wrapped by rGO nanosheets, which greatly strengthens the mechanical integrity of the whole electrode, thus improving the cycling stability of the Ni(HCO<sub>3</sub>)<sub>2</sub>/rGO composite electrode.

To gain deeper insight into the energy storage mechanism of the Ni (HCO<sub>3</sub>)<sub>2</sub>, we constructed our *in situ* Raman cell as shown in Fig. 5a. The *in situ* Raman spectroscopic evolution was conducted in 2 M KOH aqueous electrolyte, which is used to evaluate the structural transformations of the Ni(HCO<sub>3</sub>)<sub>2</sub> electrode during charge/discharge process. Fig. 5b shows the Raman spectra of the Ni(HCO<sub>3</sub>)<sub>2</sub> and Ni(HCO<sub>3</sub>)<sub>2</sub>/rGO nanocomposite powders, respectively. For the Ni(HCO<sub>3</sub>)<sub>2</sub> material, a distinct peak at 1117 cm<sup>-1</sup> can be observed, which corresponds to the hydrogen carbonate HCO<sub>3</sub><sup>-1</sup> ion band [7]. For the Ni(HCO<sub>3</sub>)<sub>2</sub>/rGO nanocomposite, two additional new peaks at around 1350 and 1585 cm<sup>-1</sup>

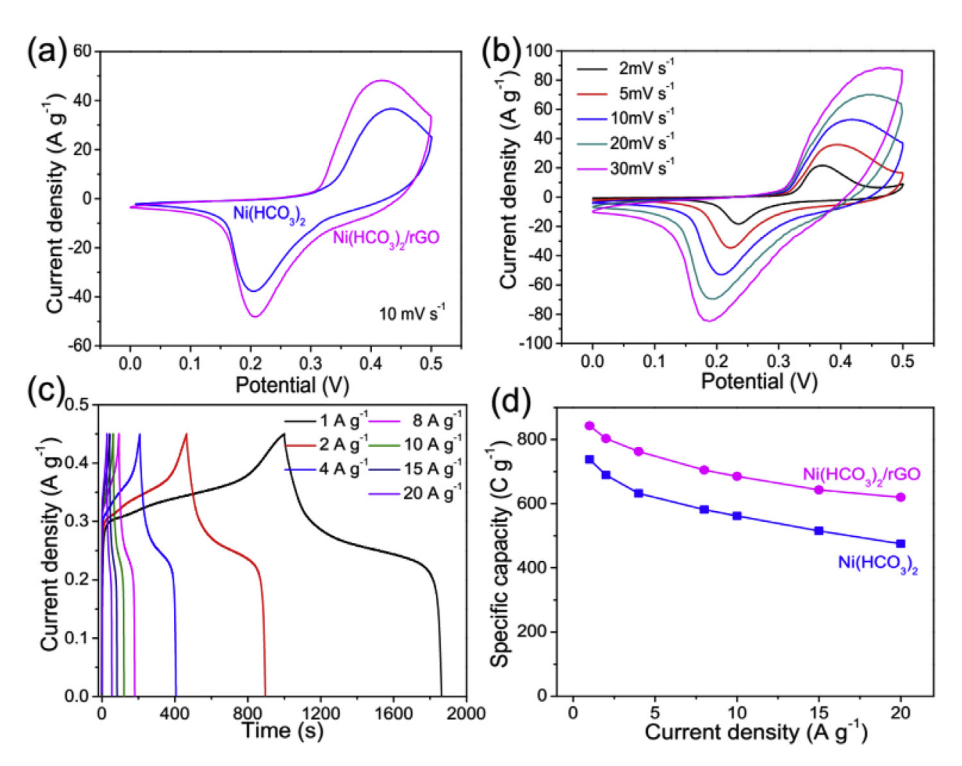


**Fig. 4.** (a) CV curves of as-synthesized Ni(HCO<sub>3</sub>)<sub>2</sub> and Ni(HCO<sub>3</sub>)<sub>2</sub>/rGO composite electrodes at  $10~\text{mV}~\text{s}^{-1}$ . (b) CV curves of as-synthesized Ni (HCO<sub>3</sub>)<sub>2</sub>/rGO composite electrode at various scan rates. (c) GCD curves of the Ni(HCO<sub>3</sub>)<sub>2</sub>/rGO composite electrode at various current densities. (d) The specific capacity of the pure Ni(HCO<sub>3</sub>)<sub>2</sub> and Ni (HCO<sub>3</sub>)<sub>2</sub>/rGO composite electrodes.

can be also observed, corresponding to the D and G bands of the rGO, respectively. Fig. 5c shows the *in situ* Raman spectroscopic evolution along with the CV curve in the voltage range of 0–0.5 V. The corresponding CV scan rate was controlled to be  $2 \text{ mV s}^{-1}$  so that one Raman spectrum could be collected in a potential interval of 0.1 V. It is noted that only one Raman band at  $1117 \text{ cm}^{-1}$  could be observed before the operating voltage was applied across the Ni(HCO<sub>3</sub>)<sub>2</sub> electrode. When the potential was increased from 0 to 0.5 V in the first cycle, three additional new bands were also observed at  $1064 (\nu_2)$ ,  $557 (\nu_3)$  and  $472 \text{ cm}^{-1} (\nu_4)$ , respectively. The  $\nu_2$  Raman band  $(1064 \text{ cm}^{-1})$  can be assigned to the (C–O) stretching vibration [28], which is attributed to the evolution of bicarbonate to carbonate in the KOH solution. The  $\nu_3$  (557 cm<sup>-1</sup>) and  $\nu_4$  (472 cm<sup>-1</sup>) bands can be assigned to the Ni–O

stretching vibration modes and proton vacancy sites, which matches very well with Raman spectrum of  $\gamma$ -NiOOH [29]. These phenomenon suggests the positive charge storage, responding to the oxidation process of Ni(HCO<sub>3</sub>)<sub>2</sub> to  $\gamma$ -NiOOH. When the potential was decreased from 0.5 to 0 V in the first cycle, the relatively weak  $\nu_3$  and  $\nu_4$  bands were also observed at 557 and  $470\,\mathrm{cm}^{-1}$ , respectively. This phenomenon implies that the oxidized Ni(HCO<sub>3</sub>)<sub>2</sub> was reduced slowly, and a portion of  $\gamma$ -NiOOH could not be reduced completely. The partial unreduced Ni<sup>3+</sup> islands distributed in the surface of Ni(HCO<sub>3</sub>)<sub>2</sub> could contribute to improving the conductivity of the whole electrode at an acceptable level [30,31]. All the results reveal a reversible transfer from the Ni (HCO<sub>3</sub>)<sub>2</sub> to NiOOH, which also further confirmed by the *in situ* Raman spectrum in the second cycle process. Moreover, it should be noted that

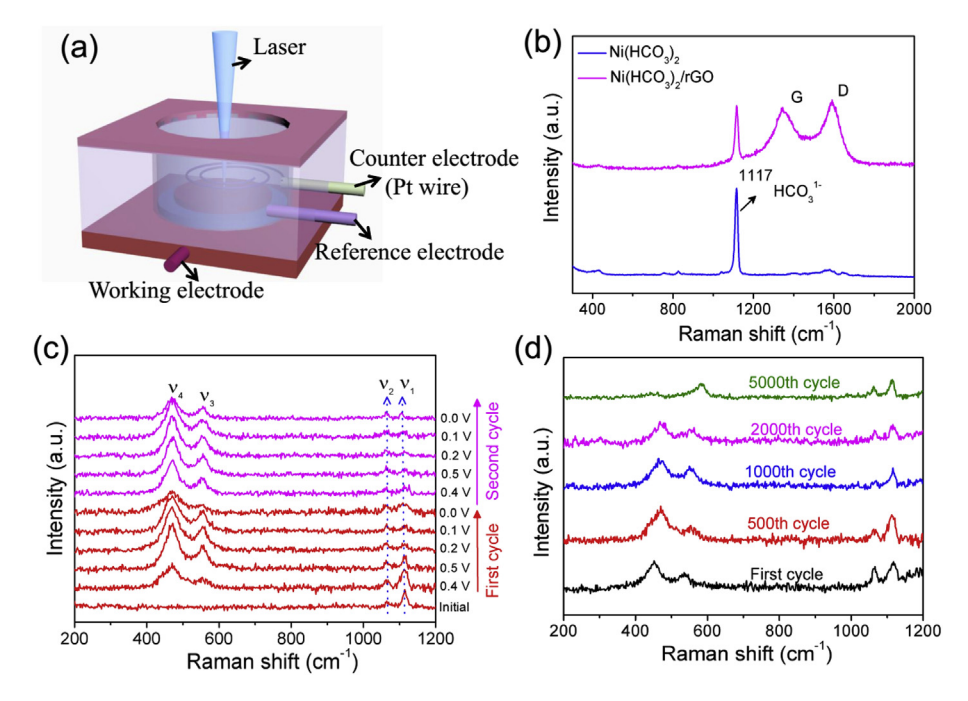


Fig. 5. (a) Detailed construction of the  $in \, situ \, Raman$  cell used in this study. (b) Raman spectra of the Ni (HCO<sub>3</sub>)<sub>2</sub> and Ni(HCO<sub>3</sub>)<sub>2</sub>/rGO powders with equivalent laser power of 10 mW. (c)  $In \, situ \, Raman \, spectra$  evolution of the Ni(HCO<sub>3</sub>)<sub>2</sub> thin film acquired at different states of charge/discharge in 2 M KOH electrolyte. (d)  $In \, situ \, Raman \, spectra \, evolution \, of the Ni(HCO<sub>3</sub>)<sub>2</sub> thin film acquired at different charge/discharge cycles.$ 

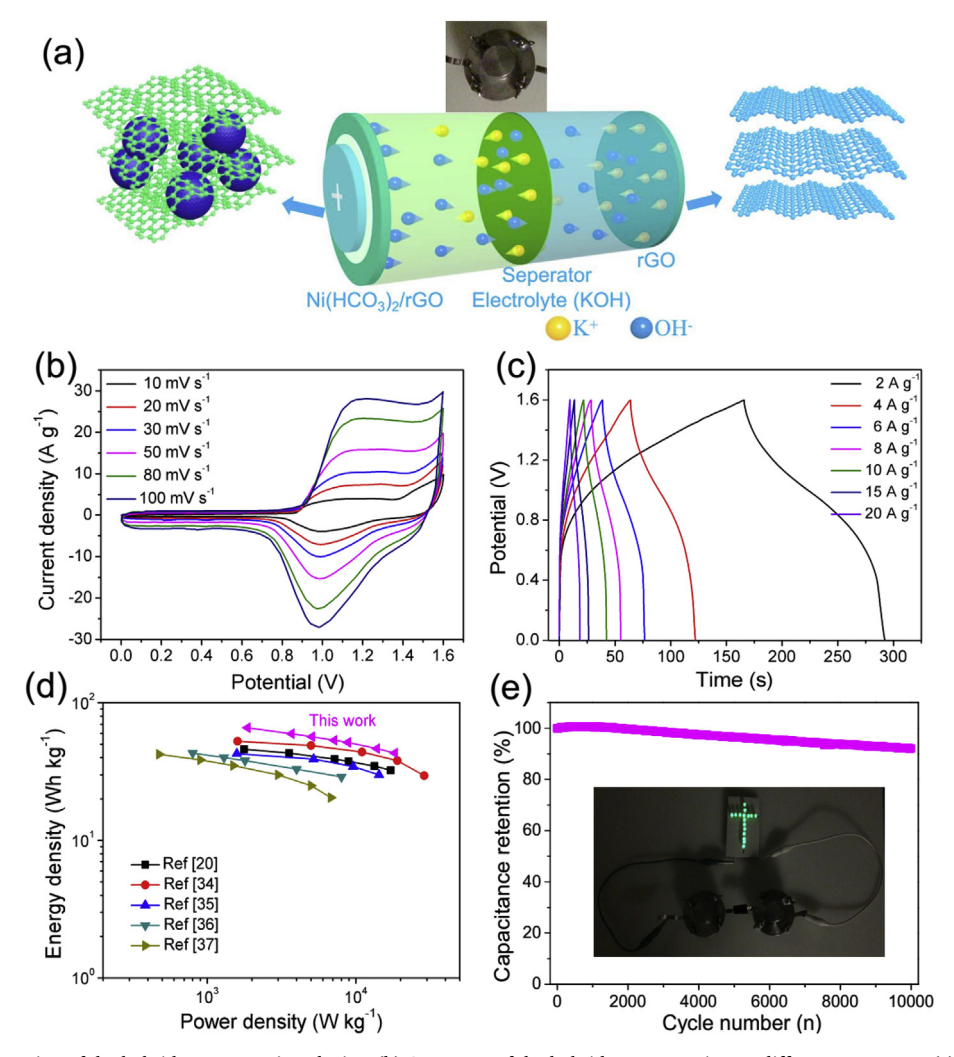


Fig. 6. (a) Schematic illustration of the hybrid supercapacitor device. (b) CV curves of the hybrid supercapacitor at different scan rates. (c) GCD curves of the hybrid supercapacitor at different current densities. (d) Ragone plots of the hybrid supercapacitor. (e) Cycling performance of the hybrid supercapacitor. Inset shows the digital photograph of 16 LEDs lighted by two hybrid supercapacitors connected in series.

the  $\nu_4$  stretching mode exhibits a blue shift from 470 to 472 cm<sup>-1</sup> with the applied potential from 0 V to 0.5 V. This phenomenon clearly indicates massive positive charge storage lead to the stiffening of  $\nu_4$ stretching mode, implying the shortening of Ni-O bond [11]. Reversibly, the phenomenon of red shift (472–470 cm<sup>-1</sup>) of  $\nu_4$  stretching mode was observed with the applied potential from 0.5 V to 0 V, which implies the release of the stored positive charge restored the Ni-O bond length [11]. Furthermore, the in situ Raman spectroscopic evolution was also collected during a long charge-discharge cycling process, and the responding current density was about  $10\,\mathrm{A\,g}^{-1}$ . As shown in Fig. 5d, the obtained Raman bands were almost unchanged before the first 2000 cycles, which further proves the reversible redox reaction and good cycle stability of the electrode in the early stages of the chargedischarge process. However, when the charge-discharge cycle was close to the 5000th or higher, the obtained Raman spectrum has changed significantly. The  $\nu_4$  band almost disappeared, and the  $\nu_3$  band was blue shifted from 557 to 581 cm<sup>-1</sup>, which could be attributed to the conversion of γ-NiOOH to the disordered β-NiOOH with aging [32]. Owing to the unstable of the y-phase in KOH electrolyte, a portion of unreduced γ-NiOOH was converted into the β-NiOOH, thus leading to the transformation of the β-NiOOH to β-Ni(OH)2 in the subsequent discharge process [33]. To confirm the structural evolution of Ni(HCO<sub>3</sub>)<sub>2</sub> during the long-term cycling, the ex-situ XRD have been also performed and the results are shown in Fig. S6. Obviously, no new diffraction

peaks were observed during the early cycles, suggesting the good reversible redox reaction of the electrode in the early stages. With the increasing of charge-discharge cycles, three new diffraction peaks can be clearly observed at  $2\theta = 19.2^{\circ}$ ,  $33.1^{\circ}$  and  $39.1^{\circ}$ , which can be indexed as the (001), (100) and (002) planes of β-Ni(OH)<sub>2</sub>, respectively (JCPDS, 14-0117). Besides, the intensity of these three new diffraction peaks gradually increased with long-term cycles, further revealing the final phase transformation of Ni(HCO<sub>3</sub>)<sub>2</sub> into disordered β-Ni(OH)<sub>2</sub>. The electrochemically induced irreversible phase transformation of Ni (HCO<sub>3</sub>)<sub>2</sub> into β-Ni(OH)<sub>2</sub> reduced the reaction kinetics, and hindered the diffusion of ions, thus arousing the poor electrochemical properties of the whole electrode, which could be further proved by the in suit EIS measurement as the reaction proceeds. As shown in Figs. S7a and b, the charge transfer resistance of the Ni(HCO<sub>3</sub>)<sub>2</sub> electrode was almost unchanged at the charging stage of 0-0.3 V, and then gradually decreased at the charging stage of 0.3-0.5 V. Contrarily, it would gradually increase during the whole discharge process (0.5–0 V). It is noted that the charge transfer resistance of the Ni(HCO<sub>3</sub>)<sub>2</sub> electrode retained the smallest at the end of the charging (0.5 V), which further revealed that the oxidized y-NiOOH islands distributed in the surface of Ni(HCO<sub>3</sub>)<sub>2</sub> could improve the conductivity of the electrode. However, when the electrode was discharged to 0 V, the charge transfer resistance of the electrode was higher than its initial state, which suggests that a partial transformation of disordered β-Ni(OH)<sub>2</sub> may hinder the transmission of

electrons. Moreover, the charge transfer resistance measured at the end of the charging (0.5 V) would gradually increase with the increasing of charge-discharge cycles, and eventually higher than the initial state (Fig. S8). Besides, the interfacial resistance would gradually increase during the long-term cycles, suggesting that the transformation of Ni (HCO<sub>3</sub>)<sub>2</sub> into β-Ni(OH)<sub>2</sub> could hinder the diffusion of ions. All these results indicate that the irreversible phase transformation of γ-NiOOH into disordered β-Ni(OH)<sub>2</sub> can reduce the electrochemical performance of the Ni(HCO<sub>3</sub>)<sub>2</sub> electrode. Therefore, an ideal energy storage electrode material need to a good design and construction, which can retard its structural degradation or even maintain its intrinsic structure without change during the long charge-discharge process. Compared with the Ni(HCO<sub>3</sub>)<sub>2</sub>, the Raman spectra (Fig. S9) of Ni(HCO<sub>3</sub>)<sub>2</sub>/rGO electrode reveal that the presence of rGO can strengthen the intrinsic structure of Ni(HCO<sub>3</sub>)<sub>2</sub> nanomaterials, and improve its cycling stability. As shown in Fig. S10, only three bands were observed at 1117, 557 and 472 cm<sup>-1</sup> during the whole charge-discharge process in the early cycles. The Raman band at 1064 cm<sup>-1</sup> could be only observed after a long-term charge-discharge cycles, meanwhile, the shapes of the Raman bands (1117, 557 and 472 cm<sup>-1</sup>) did not significantly change even after 5, 000 cycles (Fig. S10). All the results further proves that the rGO can retard the structural degradation of Ni(HCO<sub>3</sub>)<sub>2</sub> nanomaterials.

To further evaluate the viability of the Ni(HCO<sub>3</sub>)<sub>2</sub>/rGO nanocomposite for practical application, a hybrid supercapacitor device was constructed by using the Ni(HCO<sub>3</sub>)<sub>2</sub>/rGO composite as anode and the rGO as cathode, as schematically shown in Fig. 6a. According to the CV test for the individual Ni(HCO<sub>3</sub>)<sub>2</sub>/rGO and rGO electrodes (Fig. S11), the mass ratio of the anode to the cathode is about 0.33 to balance the charge between the two electrodes (for detailed information about the cathode, see Fig. S12). Fig. S13 displays the CV curves of as-fabricated HSC at various operating voltage windows. Obviously, the integral area increases with the increase of voltage windows (0-1.6 V), suggesting that higher capacitance was achieved. However, a further increase of the maximum operating voltage to 1.8 V resulted in a dramatic increase of current density, which could be attributed to electrolyte decomposition/water splitting. Thus, the optimum operating voltage window of as-fabricated HSC device was 1.6 V. The shape of all CV curves (Fig. 6b) could be well maintained at various scan rates, indicating high rate performance of the HSC. The corresponding GCD curves of asfabricated HSC device at different current densities are displayed in Fig. 6c. The GCD curves remain in good symmetry at cell voltage as high as 1.6 V, indicating good electrochemical reversibility of as-fabricated HSC device. As shown in Fig. 6d, the Ragone plot indicates the relationship between the energy and power density of the HSC device. The HSC device delivered an ultrahigh energy density of 66 Wh  ${\rm kg}^{-1}$  at 1.9 kW kg<sup>-1</sup>. Moreover, an energy density of 43 Wh kg<sup>-1</sup> can be retained even at a high power density of 18.8 kW kg<sup>-1</sup> with a discharge time of 8.3 s, demonstrating its ultrafast energy storage capability. The performance of as-fabricated HSC were superior to many systems reported previously, such as Ni-Co oxide//G/MMCS (52.6 Wh kg<sup>-1</sup> at  $1.6 \, kW \, kg^{-1}$ ) [34], NiCo<sub>2</sub>S<sub>4</sub>//AC (42.7 Wh kg<sup>-1</sup> at  $1.6 \, kW \, kg^{-1}$ ) [35], NiS-Ni<sub>3</sub>S<sub>2</sub>-Ni<sub>3</sub>S<sub>4</sub>/rGO//graphene (46 Wh kg<sup>-1</sup> at  $1.8 \, kW \, kg^{-1}$ ) [20], Ni-Co-S/G//PCNS (43.2 Wh  $kg^{-1}$  at 0.8 kW  $kg^{-1}$ ) [36], NiCo<sub>2</sub>S<sub>4</sub>// graphene (42.3 Wh kg $^{-1}$  at 0.5 kW kg $^{-1}$ ) [37]. As shown in Fig. 6e, the cycling life of the HSC is very impressive as well, retaining 92% of its initial capacitance over 10,000 cycles at 20 A g<sup>-1</sup>, which is comparable or even superior to those recently reported for advanced hybrid/ asymmetric SCs in the literature [37-41]. Furthermore, two such HSC devices connected in series can power 16 LEDs after being charged to 3.2 V (Fig. 6e, Inset), indicating its good practical application (the corresponding video file in supporting information).

Supplementary video related to this article can be found at https://doi:10.1016/j.nanoen.2019.103919

#### 4. Conclusion

In summary, we have successfully synthesized Ni(HCO<sub>3</sub>)<sub>2</sub> nanoparticles with a good distribution wrapped by rGO nanosheets for high performance SCs. Moreover, the energy storage mechanism of Ni (HCO<sub>3</sub>)<sub>2</sub> was explored by the in situ Raman spectroscopy. It was found that the high specific capacity of Ni(HCO<sub>3</sub>)<sub>2</sub> was attributed to the deep oxidation of Ni(HCO<sub>3</sub>)<sub>2</sub> to  $\gamma$ -NiOOH, but the oxidized  $\gamma$ -NiOOH could not be completely reduced in one charge-discharge cycle, and the partial Ni<sup>3+</sup> cations could be reduced in the next cycle. The early reaction process did not affect the electrochemical performance of the Ni (HCO<sub>3</sub>)<sub>2</sub> electrode. However, the partial phase transformation of y-NiOOH into disordered β-Ni(OH)<sub>2</sub> during the long charge-discharge cycles, which are most likely responsible for the electrode capacity loss. This irreversible phase change damaged the crystal structure of Ni (HCO<sub>3</sub>)<sub>2</sub>, hindered the electronic transport and electrolyte ionic diffusion through the whole electrode system, thus leading to the capacity fading and poor cycle performance. The optimized Ni(HCO<sub>3</sub>)<sub>2</sub>/rGO composite electrode delivered an ultrahigh specific capacity, good rate capability, high energy density and good cycling stability.

## Acknowledgements

This work was supported by the National Natural Science Foundation of China (Grant No. 21805247), the Henan provincial key science and technology research projects(Grant No. 192102210040), the China Postdoctoral Science Foundation (Grant No. 2018M630831), the Youth Teacher Start Fund of Zhengzhou University (Grant No.32210813), the US National Science Foundation under award number DMR-1410320 and DMR-1742828.

#### Appendix A. Supplementary data

Supplementary data to this article can be found online at https://doi.org/10.1016/j.nanoen.2019.103919.

#### References

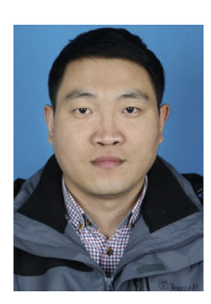
- [1] S. Chu, A. Majumdar, Nature 488 (2012) 294-303.
- [2] B. Dunn, H. Kamath, J.M. Tarascon, Science 334 (2011) 928–935.
- [3] D.C. Chen, J.H. Wang, T.F. Chou, B.T. Zhao, M.A. El-Sayed, M.L. Liu, J. Am. Chem. Soc. 139 (2017) 7071–7081.
- [4] S.G. Dai, W.N. Xu, Y. Xi, M.J. Wang, X. Gu, D.L. Guo, C.G. Hu, Nano Energy 19 (2016) 363–372.
- [5] Q.X. Xia, K.S. Hui, K.N. Hui, S.D. Kim, J.H. Lim, S.Y. Choi, L.J. Zhang, R.S. Mane, J.M. Yunf, K.H. Kim, J. Mater. Chem. A 3 (2015) 22102–22117.
- [6] Q.B. Zhang, Z.C. Liu, B. Zhao, Y. Cheng, L. Zhang, H.H. Wu, M.S. Wang, S.G. Dai, K.L. Zhang, D. Ding, Y.P. Wu, M.L. Liu, Energy Storage Mater. 16 (2019) 632–645.
- 7] S.Q. Zhao, Z.W. Wang, Y.J. He, B.B. Jiang, Y.W. Harn, X.Q. Liu, F.Q. Yu, F. Feng, Q. Shen, Z.Q. Lin, ACS Energy Lett. 2 (2017) 111–116.
- [8] J.M. Gu, X. Liu, Z. Wang, Z.P. Bian, C.H. Jin, X. Sun, B.P. Yin, T.H. Wu, L. Wang, S.F. Tang, H.C. Wang, F.M. Gao, Nanotechnology 28 (2017) 345401.
- [9] Y.T. Dong, Y.H. Ma, D. Li, Y.S. Liu, W.H. Chen, X.M. Feng, J.M. Zhang, Chem. Sci. 9 (2018) 8682–8691.
- [10] C. Qu, B. Zhao, Y. Jiao, D.C. Chen, S.G. Dai, B.M. deglee, Y. Chen, K.S. Walton, R.Q. Zou, M.L. Liu, ACS Energy Lett. 2 (2017) 1263–1269.
- [11] D.C. Chen, X.H. Xiong, B. Zhao, M.A. Mahmoud, M.A. El-Sayed, M.L. Liu, Adv. Sci. 3 (2016) 1500433.
- Q.B. Zhang, H.X. Chen, L.L. Luo, B. Zhao, H. Luo, X. Han, J.W. Wang, C.M. Wang, Y. Yang, T. Zhu, M.L. Liu, Energy Environ. Sci. 11 (2018) 669–681.
  R. Zhang, Y. Zhang, Z.C. Dong, S. Jiang, C. Zhang, L.G. Chen, L. Zhang, V. Liao
- [13] R. Zhang, Y. Zhang, Z.C. Dong, S. Jiang, C. Zhang, L.G. Chen, L. Zhang, Y. Liao, J. Aizpurua, Y. Luo, J.L. Yang, J.G. Hou, Nature 498 (2013) 82–86.
- [14] J.F. Li, X.D. Tian, S.B. Li, J.R. Anema, Z.L. Yang, Y. Ding, Y.F. Wu, Y.M. Zeng, Q.Z. Chen, B. Ren, Z.L. Wang, Z.Q. Tian, Nat. Protoc. 8 (2013) 52–65.
- [15] A.C. Ferrari, D.M. Basko, Nat. Nanotechnol. 8 (2013) 235-246.
- [16] L.F. Yang, S. Cheng, J.H. Wang, X. Ji, Y. Jiang, M.H. Yao, P. Wu, M.K. Wang, J. Zhou, M.L. Liu, Nano Energy 30 (2016) 293–302.
- [17] D.C. Marcano, D.V. KosynKin, J.M. Berlin, A. Sinitskii, Z.Z. Sun, A. Slesarev, L.B. Alemany, W. Lu, J.M. Tour, ACS Nano 4 (2010) 4806–4814.
- [18] T. Brousse, D. Belanger, J.W. Long, J. Electrochem. Soc. 162 (2015) A5185–A5189.
- [19] L.Q. Mai, A. Khan1, X.C. Tian, K.M. Hercule, Y.L. Zhao, X. Lin, X. Xu, Nat. Commun. 4 (2013) 2923.
- [20] S.G. Dai, B. Zhao, C. Qu, D.C. Chen, D. Dang, B. Song, B.M. deGleea, J.W. Fu, C.G. Hu, C.P. Wong, M.L. Liu, Nano Energy 33 (2017) 522–531.

[21] J.H. Li, Z.C. Liu, Q.B. Zhang, Y. Cheng, B. Zhao, S.G. Dai, H.H. Wu, K.L. Zhang, D. Ding, Y.P. Wu, M.L. Liu, M.S. Wang, Nano Energy 57 (2019) 22–33.

- [22] J.F. Sun, Z.P. Li, J.Q. Wang, Z.F. Wang, L.Y. Niu, P.W. Gong, X.H. Liu, H.G. Wang, S.R. Yang, J. Alloy. Comp. 581 (2013) 217–222.
- [23] J.J. Tian, Y. Xue, M.M. Wang, Y.C. Pei, H.C. Zhang, J.J. Wang, Electrochim. Acta 296 (2019) 49–58.
- [24] Y.T. Dong, Y.H. Ma, D. Li, Y.S. Liu, W.H. Chen, X.M. Feng, J.M. Zhang, Chem. Sci. 9 (2018) 8682–8691.
- [25] C. Qu, L. Zhang, W. Meng, Z.B. Liang, B.J. Zhu, D. Dang, S.G. Dai, B. Zhao, H. Tabassum, S. Gao, H. Zhang, W.H. Guo, R. Zhao, X.Y. Huang, M.L. Liu, R.Q. Zou, J. Mater. Chem. A 6 (2018) 4003–4012.
- [26] C. Qu, Z.B. Liang, Y. Jiao, B. Zhao, B.J. Zhu, D. Dang, S.G. Dai, Y. Chen, R.Q. Zou, M.L. Liu, Small (2018) 1800285.
- [27] W. Xia, C. Qu, Z.B. Liang, B. Zhao, S.G. Dai, B. Qiu, Y. Jiao, Q.B. Zhang, X.Y. Huang, W.H. Guo, D. Dang, R.Q. Zou, D.G. Xia, Q. Xu, M.L. Liu, Nano Lett. 17 (2017) 2788–2795.
- [28] R.L. Frost, M.J. Dickfos, B.J. Reddy, J. Raman Spectrosc. 39 (2008) 1250-1256.
- [29] S. Klaus, Y. Cai, M.W. Louie, L. Trotochaud, A.T. Bell, J. Phys. Chem. C 119 (2015) 7243–7254.
- [30] M.C. Bernard, M. Keddcim, H. Takenouti, J. Electrochem. Soc. 143 (1996) 2447–2451.
- [31] J.L. Bantignies, S. Deabate, A. Righi, S. Rols, P. Hermet, J.L. Sauvajol, F. Henn, J. Phys. Chem. C 112 (2008) 2193–2201.
- [32] R. Kostecki, F. McLarnon, J. Electrochem. Soc. 144 (1997) 485-493.
- [33] C. Léger, C. Tessier, M. Ménétrier, C. Denage, C. Delmas, J. Electrochem. Soc. 146 (1999) 924–932.
- [34] B.Y. Guan, A. Kushima, L. Yu, S. Li, J. Li, X.W. Lou, Adv. Mater. 29 (2017) 1605902.
- [35] B.Y. Guan, L. Yu, X. Wang, S.Y. Song, X.W. Lou, Adv. Mater. 29 (2017) 1605051.
- [36] J. Yang, C. Yu, X.M. Fan, S.X. Liang, S.F. Li, H.W. Huang, Z. Ling, C. Hao, J.S. Qiu, Energy Environ. Sci. 9 (2016) 1299–1307.
- [37] L.F. Shen, L. Yu, H.B. Wu, X.Y. Yu, X.G. Zhang, X.W. Lou, Nat. Commun. 6 (2015) 6694.
- [38] Y.Z. Chen, W.K. Pang, H.H. Bai, T.F. Zhou, Y.N. Liu, S. Li, Z.P. Guo, Nano Lett. 17 (2017) 429–436.
- [39] B. Li, P. Gu, Y.C. Feng, G.X. Zhang, K.S. Huang, H.G. Xue, H. Pang, Adv. Funct. Mater. 27 (2017) 1605784.
- [40] C. Guan, X.M. Liu, W.N. Ren, X. Li, C.W. Cheng, J. Wang, Adv. Energy Mater. 7 (2017) 1602391.
- [41] B. Zhao, L. Zhang, Q.B. Zhang, D.C. Chen, Y. Cheng, X. Deng, Y. Chen, R. Murphy, X.H. Xiong, B. Song, C.P. Wong, M.S. Wang, M.L. Liu, Adv. Energy Mater. (2017) 1702247



Shuge Dai is currently an associate professor at School of Physics and Engineering, Zhengzhou University. He received his Ph.D degree from the Department of Applied Physics at Chongqing University of China. He joined Prof. Meilin Liu's group as a visiting student at School of Materials Science and Engineering, Georgia Institute of Technology in 2015. His research interests mainly focus on the efficient energy storage and conversion, including supercapacitors, nanogenerators, lithium ion batteries.



Zhuangfei Zhang is currently an associate professor at school of Physics and Engineering, Zhengzhou University. He received his Ph.D. degree from the Department of Condensed Matter Physics at JiLin University of China. His research interests mainly focus on the high pressure synthesis of functional materials, including superhard materials, thermoelectric materials and battery materials.



Junmin Xu received his Ph.D. degree in Condensed Matter Physics from Institute of Solid State Physics (ISSP), Chinese Academy of Science (CAS) in 2013. Now, he is working at Department of Physics and Engineering, Zhengzhou University. His research interests focus on design and synthesis of novel nanomaterials and nanostructures for energy storage applications.



Weixia Shen is currently an assistant engineer at school of Physics and Engineering, Zhengzhou University. She received her M.S degree from the Department of Condensed Matter Physics at Jilin Normal University of China. Her research interests mainly focus on the in-suit Raman and Infrared performance tests, including lithium ion batteries, supercapacitors.



Qiaobao Zhang is currently an Assistant Professor in the Department of Materials Science and Engineering at Xiamen University. He obtained his M.S. degree from City University of Hong Kong (supervised by Prof Kaili Zhang) in 2016. He joined Prof. Meilin Liu's group as a visiting Ph.D. student in Georgia Institute of Technology in 2015. His current research includes developing nanostructured materials for electrochemical energy storage devices such as Li/Na ion batteries and supercapacitors and investigating their energy storage mechanism by *in situ* SEM/TEM. His research results have been published in Progress in Materials Science, Energy & Environmental Science, Advanced Energy Materials, ACS Nano, Nano Letters,

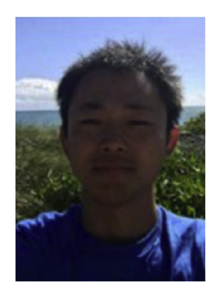
Nature Communications, Science Advances, Nano Energy, Energy Storage Materials, Small, Journal of Materials Chemistry A, etc.



Xigui Yang received his Ph.D. (2017) in State Key Laboratory of Superhard Materials from Jilin University. He now works in the department of physics and engineering in Zhengzhou University. His research focuses on the structure-property relationships of functional materials under high pressure.



Tingting Xu received her Ph.D. degree in School of Physics Science and Engineering from Beijing University in 2014. She is currently an associate professor in Zhengzhou University, China. Her current research interests are mainly focused on using transmission electron microscopy as designing tool for novel energy materials.



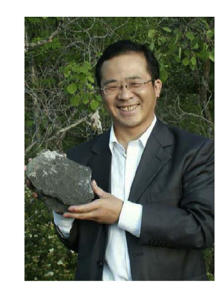
Dai Dang is currently a an associate professor at School of Chemical Engineering and Light Industry, Guangdong University of Technology. He received his Ph.D. degree in South China University of Technology under supervision of Prof. Shijun Liao in 2017. He received his bachelor degree from South China University of Technology in 2011. He joined Prof. Meilin Liu's group as a joint Ph.D. student in Georgia Institute of Technology in 2015. His research interests mainly focus on electrocatalysts for PEM fuel cells and intermediate temperature fuel cells.



Jianwei Fu is currently an associate professor at School of Materials Science and Engineering, Zhengzhou University. He received his B.S. and M.S. degree from Zhengzhou University and Ph.D. degree from Shanghai Jiao Tong University, China. His research interests include rational design of nanostructured carbon materials for efficient energy storage and conversion, and synthesis of polymorphic polymer micro- and nanomaterials and their application in dye adsorption and catalysis.



Hao Hu received his double Bachelor's degree in Physics and Applied Chemistry at Central China Normal University in 2012. He is currently pursuing his Ph.D. under the supervision of Prof. Ying Yu in the Institute of Nano-Science and Nano-Technology at Central China Normal University. He joined Prof. Meilin Liu's group as a joint Ph.D. student at School of Materials Science and Engineering, Georgia Institute of Technology in November 2016. His research interests mainly focus on the efficient energy storage and conversion, including supercapacitors, metal ion batteries and interface electrochemistry.



Xinjian Li is a professor of physics in Zhengzhou University, and Associate Chair of School of Physics and Engineering. He received his Ph.D. degree from University of Science and Technology of China in 1999. His research interests include the preparation and characterization of silicon-based nanophotovoltaic materials and their composite nanosystems, physical property testing, physical mechanism research and prototype devices (such as light-emitting diodes, solar cells).



Bote Zhao is currently a postdoctoral fellow in the School of Materials Science and Engineering at Georgia Institute of Technology, USA. He received his B.S. And Ph.D. from Nanjing Tech University, China. His research experiences include binder-free films, nanostructured materials, and graphene-based materials for lithium ion batteries and supercapacitors, electrospinning synthesis of fibers, fabrication and water management of proton exchange membrane fuel cells, and hydrogen production from hydrous hydrazine. He is currently focusing on the synthesis and characterization of novel materials for batteries, fuel cells, and supercapacitors.



Chenguo Hu is a professor of physics in Chongqing University and the director of Key Lab of Materials Physics of Chongqing Municipality. She received her Ph. D. in Materials from Chongqing University in 2003. Her research interests include methodology of synthesizing functional nanomaterials, investigation of morphology and size dependent physical and chemical properties of nanomaterials, and design and fabrication of electronic devices, such as nanogenerators and sensors.



Ye Wang received his Master of Science degree from University of Science and Technology of China (USTC), HeFei, China, in 2007, and the Ph.D degree from the Nanyang Technology University (NTU), Singapore, in 2013. He has authored or coauthored more than 40 publications in international journals and 1 US patent. His research interests include energy storage devices and optoelectrical devices, including lithium/sodium ion batteries, supercapacitors and thin film transistors etc.



Meilin Liu is a B. Mifflin Hood Chair, Regents' Professor, and Associate Chair of Materials Science and Engineering and Co-Director of the Center for Innovative Fuel Cell and Battery Technologies at Georgia Institute of Technology, Atlanta, Georgia, USA. He received his BS from South China University of Technology and both MS and Ph.D. from University of California at Berkeley. His research interests include insitu/operando characterization and multi-scale modeling of charge and mass transfer along surfaces, across interfaces, and in membranes, thin films, and nanostructured electrodes, aiming at achieving rational design of materials and structures with unique functionalities for efficient energy storage and conversion.



Chong Qu is currently a Ph.D. candidate under supervision of Prof. Ruqiang Zou, Peking University. He received his bachelor degree from School of Chemistry and Chemical Engineering at Nanjing University in 2013. He joined Prof. Meilin Liu's group as a GT-PKU joint program student at School of Materials Science and Engineering, Georgia Institute of Technology in 2014. His research interests include electrochemical materials based on crystalline porous frameworks for supercapacitors and Li-ion battery.